

# Constraints from ISO Data on the Velocity Law and Clumpiness of WR 136<sup>1</sup>

R. Ignace, M. F. Quigley, and J. P. Cassinelli

*Department of Astronomy, University of Wisconsin, Madison, WI 53706-1582*

ignace@astro.wisc.edu, quigley@astro.wisc.edu, cassinelli@astro.wisc.edu

## ABSTRACT

Observations with the Infrared Space Observatory (ISO) SWS spectrometer are used to constrain the velocity law and wind clumping of the well-studied Wolf-Rayet (WR) star WR 136 (HD 192163) (WN6). Because the free-free continuum opacity in WR winds increases steadily with wavelength in the IR, each point in the continuous spectrum may be regarded as forming in a pseudo-photosphere of larger radius for longer wavelength. Using this idea in combination with an analysis of the Doppler-broadened widths of several He II recombination lines, we can derive information about the velocity law and clumpiness of the stellar wind of WR 136. The observed line emission emerges from the region exterior to the radius of optical depth unity in the free-free opacity, corresponding to  $v \gtrsim 0.3v_\infty$  for our shortest wavelength line. The ISO observations provide the continuum shape, flux level, and seven fairly strong He II emission profiles. Adopting a  $\beta$ -law distribution for the outflow velocity law, we compute the continuous energy distribution and line profiles. We find that there is a broad range of  $\beta$ -values consistent with the continuum data if we also allow the wind temperature to be a free parameter. Interestingly, the continuum data are found to constrain the wind to have fairly low clumping values for the IR-forming region. Using the continuum results in conjunction with line profile modeling, the observational constraints are best satisfied with a clumping factor of  $D_c = \langle \rho^2 \rangle / \langle \rho \rangle^2$  of 1–3 and a  $\beta$ -value of 2–3, although higher  $\beta$  values are not strongly ruled out for a modest wind temperature. The wavelength range of our ISO data allows us to probe only the outer wind acceleration zone, but in combination with radio observations, our finding that the wind clumping is fairly small suggests that the clumping in the wind of WR 136 decreases with increasing radius.

*Subject headings:* Infrared: stars, Stars: individual: WR 136, Stars: winds, Stars: line formation, Stars: Wolf-Rayet

## 1. INTRODUCTION

The Wolf-Rayet (WR) class of early-type stars has long been known for having extreme stellar wind properties. In the visible band, broad emission lines that form in the wind dominate the stellar spectrum (Abbott & Conti 1987). The explanation of these extreme outflows has long posed se-

vere problems for stellar wind theories. In particular these stars are noted for their “wind momentum problem” (Barlow *et al.* 1981; Abbott *et al.* 1986; Willis 1991), in which the momentum flux in the wind  $\dot{M}v_\infty$  (where  $\dot{M}$  is the mass loss rate and  $v_\infty$  is the terminal speed of the stellar wind) can exceed by more than an order of magnitude the momentum flux  $L_*/c$  (where  $L_*$  is the stellar Bolometric luminosity) of the radiation field purportedly responsible for the outflows. This situation is normally parametrized by the performance number  $\eta = \dot{M}v_\infty c/L_*$ , which is of order 10 for WR stars (although there can be a wide range –

<sup>1</sup>Based on observations with ISO, an ESA project with instruments funded by ESA Member States (especially the PI countries: France, Germany, the Netherlands, and the United Kingdom) and with the participation of ISAS and NASA.

see Hamann & Koesterke 1998). In recent years the observational estimates of WR wind momenta have been reduced, partly from upward revisions of stellar luminosities (by line blanketing, e.g., Hillier & Miller 1999) and partly by accounting for clumpiness in the winds (Hillier 1991; Hamann & Koesterke 1998), yet values of  $\dot{M}v_\infty$  remain large ( $\approx 10$ , Nugis & Lamers 2000).

Alternative wind-driving mechanisms have been proposed to explain the large wind momenta, but several studies have indicated that the WR winds can be driven by radiative forces alone, without invoking other physics (such as magnetic fields), through multi-line scattering of the stellar radiation field (Lucy & Abbott 1993; Springmann 1994; Gayley, Owocki, & Cranmer 1995; Onifer & Gayley 2003). Multi-line scattering is possible because of ionization gradients in the wind flow. As photons escape from the inner wind with an opacity characterized by a particular distribution of lines, the photons encounter different sets of line opacities at larger radii because of changes in the dominant ions. Indeed a wide range in ionization states as a function of radius appears to exist in the WR winds (Kuhi 1973; Schulte-Ladbeck, Eenens, & Davis 1995; Herald *et al.* 2000). Thus there can be a greater deposition of momentum by the stellar radiation field to drive the wind, and an enhancement of the wind momentum flux.

Although multi-line scattering can influence the mass-loss rates of some O stars, it tends to be much less important than for the WR stars (Vink, de Koter, & Lamers 2000). As we argue below, one of the consequences of multi-line scattering in the wind is that the rate at which the wind velocity increases with radius should be shallower in WR winds than in typical O stars. Observational constraints on the velocity laws of WR stars should thus provide a test of the multi-line scattering wind acceleration process. Obtaining such information has been the motivation for this observational study.

For early type stars, it is traditional to describe the wind velocity distribution as a function of radius using the “ $\beta$  velocity law”, which typically has the form,

$$v(r) = v_\infty \left(1 - \frac{R_*}{r}\right)^\beta. \quad (1)$$

This formula for the velocity distribution was derived with  $\beta = 0.5$  in one of the earliest of radiation-driven outflow models by Milne (1926). The same value was predicted in the line-driven wind theory of Castor, Abbott, & Klein (1975; CAK). In detailed modeling of Of and OB supergiants by Groenewegen & Lamers (1989), values of  $\beta = 0.7\text{--}0.9$  were found. These higher values indicate a shallower rise in the velocity distribution versus radius and are also in better agreement with the predictions of the modified CAK (mCAK) theory of Friend & Abbott (1986) and Pauldrach, Puls, & Kudritzki (1986). These mCAK models accounted for the finite size of the star producing the wind. They also led to predictions for  $\dot{M}$  and  $v_\infty$  that are in good agreement with observations of O stars. The difference in the  $\beta$  values in going from the CAK to the mCAK model arises from the fact that the angular distribution of the driving radiation field is different. For the very forward-peaked radiation field of CAK, the acceleration is rapid, but for the somewhat more dispersed radiation field associated with the finite disks of mCAK, the velocity law is shallower. The multi-line scattering leads to an even less strongly forward-peaked radiation field and to yet another step away from a point-like radiation field. Thus it is to be expected that the velocity law for WR stars should have even higher values of  $\beta$ .

With the view that multi-line scattering can lead to a significant enhancement of the winds, momentum transfer is no longer the major issue in understanding the large mass-loss rates of WR stars. Instead there is now a need for the opacity to adequately “trap” or prevent the leakage of the photons so that multi-line scattering can indeed occur. As the photons transmit some of their outward momentum to the wind, they are red shifted. If there are gaps in the opacity versus wavelength distribution, the photons can escape and thus contribute no further to the wind acceleration. Since the winds of WR stars require that photons transmit about  $\eta \times$  their momentum  $h\nu_0/c$  to the wind, a very large effective number of scatterings per photon is required. For example, Gayley *et al.* (1995) show in their Figure 3, that a photon will interact with approximately  $\eta^2$  lines, and experience a net redshift of  $\Delta\lambda \approx \lambda_0 (\eta v_\infty/c)$ . A photon that initially interacts with a EUV line near 600 Å will tend to drift about 660 Å redward.

Consequently, there can be few gaps in the line opacity distribution, lest photons flood through opacity minima to escape the wind before depositing sufficient momentum to the flow. Hence the wind momentum problem has now come to be interpreted as an “opacity problem” (Gayley *et al.* 1995).

Rather little is known observationally about the radial distribution of velocity in WR winds. However, a good estimate for the wind terminal speed  $v_\infty$  can be made from forbidden line profiles (e.g., Barlow, Roche, & Aitken 1988; Willis *et al.* 1997; Morris *et al.* 2000; Ignace *et al.* 2001 [hereafter Paper I]). This is because such lines are typically formed at large distances of hundreds of stellar radii or more, where the wind has achieved its asymptotic expansion speed. Because the forbidden lines are optically thin and form in the constant velocity zone, they tend to exhibit flat-topped profiles, the half-widths of which accurately determine the wind terminal speed.

Much less is known about the radial distribution of the velocity  $v(r)$  deeper in the wind. There have been several discussions about the values of  $\beta$  or the consequences of shallow velocity laws in WR stellar winds. From theoretical modeling, Schmutz (1997) arrived at a  $\beta$  ranging from 3 to 8. Monte Carlo radiation transport simulations by Springmann (1994) and Gayley *et al.* (1995) also reveal extended wind acceleration zones (not characterizable by a single  $\beta$  value). Support for these theoretical results comes from the study of binary systems by (Auer & Koenigsberger 1994). Also, Lépine & Moffat (1999) have derived large  $\beta$  values from observations of the regular motion of small emission peaks or “migrating features” that appear in WR He II emission lines. An interesting structural effect of large  $\beta$  values was discussed by Ignace, Cassinelli, & Bjorkman (1996). They found that velocity laws with modestly large values of  $\beta$  (such as  $\beta = 3$ ) are more likely to form wind-compressed zones as a result of stellar rotation. This effect was used to explain why some WR stars show intrinsic polarization (e.g., Harries, Hillier, & Howarth 1998).

To study the velocity law in WR stars further, we obtained Infrared Space Observatory (ISO) satellite observations, and in this paper we describe results from the best data set, which corresponds to WR 136. We use observations of both

the IR free-free continuum and emission profiles of He II recombination lines. In §2, we discuss in general the continuum and line diagnostics of the density and velocity distributions in WR stars. In §3, the description of the data obtained with the ISO satellite and its analysis to infer  $\beta$  is presented. The results of the study are discussed in §4.

## 2. INFRARED DIAGNOSTICS FOR DENSE STELLAR WINDS

Relative to the flows from other early-type stars, the WR winds are denser and they produce spectra that are dominated by emission lines. The understanding of these spectra involves three key elements: (a) In the optical, a major continuum opacity is electron scattering, which is gray but involves complicated thermalization effects (Mihalas 1978) (b) In the UV and EUV spectral ranges, strong line blanketing both blocks the flow of radiation and drives the wind. (c) In the IR through to the radio spectral region, it is the increasingly large free-free opacity that accounts for the IR and radio continuum excesses. The advantage of using this long wavelength spectral region to study the wind structure is that the continuum opacity increases monotonically with wavelength. For wind temperatures of a few times  $10^4$  K that are applicable to radii where the free-free continuum forms, the opacity varies as  $\lambda^3$  in the near IR, gradually shifting to a  $\lambda^2$  dependence at longer wavelengths. In the latter case, the free-free opacity is so great that the emergent radiation originates at large radii where the flow has reached terminal constant expansion-velocity. The free-free opacity is lower in the IR, and this permits radiation to emerge from the parts of the wind where the flow is still accelerating. In particular, ISO observations provides us with the spectral data that allows us to diagnose an interesting segment of the wind velocity law. There are two complementary approaches that we employ: (a) a study based on the continuous energy distribution, and (b) a study of emission line profiles formed by recombination. The latter method is, in fact, related to the first in that the continuous opacity of the wind affects the range of depths over which we receive line emission, and thus can have a strong influence on profile strengths and shapes. Consequently, we consider the continuum first, and then proceed to the emission line profiles. Many of the issues rel-

evant to the interpretation of IR observations of WR stars have been discussed in investigations similar to ours, such as Hillier, Jones, & Hyland (1983) and Hillier (1987ab) in detailed studies of WR 6 (= HD 50896 = EZ CMa).

## 2.1. IR Continuum Slope Methods

The classic approach to studying WR density and velocity distributions is to consider the continuum slope. Wright & Barlow (1975) and Panagia & Felli (1975) were the first to demonstrate that the spectral slope should vary as  $f_\nu \propto \nu^{0.6}$  (or  $f_\lambda \propto \lambda^{-2.6}$ ) for a spherical wind in constant expansion-velocity and thick in the free-free continuum. There are several informative scalings that came from these early studies and subsequent considerations. For example, Wright & Barlow showed that in the constant expansion-velocity case, the continuum emission is equivalent to a volume integral over the emissivity  $j_\nu \propto \rho^2$  with a lower bound  $R_{\nu,\text{vol}}$  determined by the radius at which the line-of-sight free-free optical depth is  $\tau_{\nu,\text{ff}} = 0.244$ . This optical depth is somewhat smaller than the 2/3 value associated with the Eddington-Barbier result for plane-parallel stellar atmospheres. Adopting an “equivalent photosphere” approach, Hillier *et al.* (1983) showed that for the observed monochromatic luminosity with  $L_\nu = 4\pi R_{\nu,\text{surf}}^2 \pi B_\nu(T_e)$ , where  $B_\nu$  is the Planck function at the wind temperature, the monochromatic radius  $R_{\nu,\text{surf}}$  corresponds to a radial depth of  $\tau_{\nu,\text{ff}} = 0.05$ . This small optical depth means that to understand the monochromatic luminosity, it is essential to account for the spatially extended nature of the wind continuum formation region.

As in Wright & Barlow (1975) and Hillier *et al.* (1983), let us compare the line-of-sight optical depths for different wind velocity laws. For the geometry depicted in Figure 1, the free-free optical depth along a ray that passes through the envelope at impact parameter  $p$  (normalized to  $R_*$ ) is given by

$$\tau_{\nu,\text{ff}}(p, z) = R_* K_{\text{ff}}(T, \nu) \int_z^\infty n_i(x) n_e(x) dz', \quad (2)$$

for  $x = \sqrt{z^2 + p^2} = r/R_*$  the normalized stellar radius,  $z = Z/R_*$  the line-of-sight coordinate toward the observer,  $n_i$  the ion number density,  $n_e$

the electron number density, and  $K_{\text{ff}}(T, \nu)$  a factor that isolates the temperature and frequency dependence of the free-free opacity. This opacity factor is given in Wright & Barlow as

$$K_{\text{ff}}(T, \nu) = 3.7 \times 10^8 Z_i^2 g_\nu(T) T^{-1/2} \nu^{-3} \times \left(1 - e^{-h\nu/kT}\right) \text{ cm}^5 \text{ K}^{1/2} \text{ Hz}^3$$

where  $Z_i$  is the rms ion charge,  $g_\nu(T)$  is the Gaunt factor,  $T$  is in K, and  $\nu$  is in Hz. We assume that  $T$  is constant throughout the continuum-formation portion of the wind, and its value is treated as a free parameter, for which we know some limiting values.

We assume a spherical radial wind and use the dimensionless radius  $x = r/R$  and velocity  $w = v/v_\infty$ . From the continuity equation, the radial distribution of density is given by

$$\rho = \frac{\dot{M}}{4\pi r^2 v(r)} = \frac{\rho_0}{x^2 w(x)}, \quad (4)$$

where the scale factor is

$$\rho_0 = \frac{\dot{M}}{4\pi R_*^2 v_\infty}, \quad (5)$$

and the normalized wind velocity distribution is

$$w(x) = \left(1 - \frac{b}{x}\right)^\beta, \quad (6)$$

for

$$b = \left[1 - \left(\frac{v_0}{v_\infty}\right)^{1/\beta}\right] \quad (7)$$

Equation (6) differs from equation (1) in that we allow for the parameter  $b \leq 1$  and provides for a finite initial value  $w_0 = v_0/v_\infty$  at the base of the wind where  $x = 1$ . To evaluate the free-free optical depth in equation(2), the electron and ion densities are related to the mass density as  $n_e = \rho/\mu_e m_H$  and  $n_i = \rho/\mu_i m_H$ , for  $\mu_e$  and  $\mu_i$  the mean molecular weight per free electron and free ion, respectively.

For illustrative purposes, let us compare two simple cases: constant expansion-velocity (i.e.,  $\beta = 0$ ) and a  $\beta = 1$  velocity law involving typical

wind acceleration versus radius. The comparison is motivated by the fact that we seek to use the observed spectral energy distribution to infer information about the wind velocity law. With these two values of  $\beta$  we gain insight into how the velocity law influences the observables, and conversely what our ISO observables can tell us about the velocity distribution.

For the constant expansion-velocity case, the line-of-sight optical depth  $\tau_{\text{ff}}(x) = \tau_{\text{ff}}(z, p = 0)$  becomes

$$\tau_{\nu, \text{ff}}(x) = \frac{1}{3} \tau_c(T, \nu) x^{-3}, \quad (8)$$

so that a specified optical depth is obtained at a radius  $x_\tau = (\tau_c/3\tau)^{1/3}$ , where the constant  $\tau_c$  collects all of the various wind, atomic, and frequency dependencies in a single parameter. The total radial optical depth down to the wind base at  $x = 1$ , is  $\tau_c/3$ . The emergent intensity from any point along the line-of-sight is  $B_\nu \exp(-\tau_{\nu, \text{ff}})$ .

For the  $\beta = 1$  velocity law, the integral for the optical depth is again analytic, giving

$$\tau_{\nu, \text{ff}}(u) = \frac{\tau_c(\nu)}{b^3} \left[ \frac{1}{1-bu} - (1-bu) + 2 \ln(1-bu) \right]. \quad (9)$$

where  $u = 1/x$ . The total line-of-sight optical depth to the wind base is  $\tau_c b^{-3} [b(2-b)/(1-b) + 2 \ln(1-b)]$ .

In Figure 2, both the optical depth and the emergent intensity  $I_\nu$  are plotted against radius for these two cases. In this example both  $K_{\text{ff}}$  and  $\rho_0$  have been held constant. There are four important points to note. (a) The total line-of-sight optical depth is greater for larger  $\beta$ , because at every radius, the flow will be slower and hence denser. (b) A fixed optical depth occurs at larger radius for larger  $\beta$ . (c) Thus the observed free-free emission emerges from larger radius for larger  $\beta$ , leading to a greater monochromatic free-free luminosity  $L_\nu$ . And (d) for a constant source function  $B_\nu(T)$ , intensities emerge from contributions over a broad range of radii. When evaluating the total flux from the unresolved source, the net effect of larger values in  $\beta$  is to steepen the wind density distribution, which in turn leads to a steeper continuum spectrum.

Instead of the “forward problem” of working

from an assumed wind velocity law toward a continuum slope, the relation between the wind expansion and observed continuum emission can be addressed with an “inverse approach”. Cassinelli & Hartmann (1977) considered the relation between the observed spectral slope and the density and temperature variations assuming power law forms, with  $\rho \propto r^{-q}$  and  $T \propto r^{-m}$ . Using the effective radius concept, they derived a relation between the power-law slope  $\nu f_\nu = \lambda f_\lambda \propto \lambda^s$  and the  $q$  and  $m$  indices as given by

$$s = \frac{6q - \frac{5}{2}m - 7}{-2q + \frac{3}{2}m + 1}. \quad (10)$$

Taking the wind to be isothermal with  $m = 0$ , equation (10) reduces to  $s = (6q - 7)/(1 - 2q)$ . For a spherical wind, inferring  $q$  for the density law is equivalent to determining the *shape* of the wind velocity distribution, although not the values of the velocity. Furthermore, given the range in wavelengths of the IR observations, the shape of the derived velocity distribution is determined over the corresponding range in continuum formation radii. More generally, the spectral slope will depend not only on the density distribution, but also on the temperature gradient, electron scattering, bound-free opacity, and wind ionization variations. The main point of this discussion is that the wind velocity law can control the continuum spectral slope and may thus be inferable from observations.

## 2.2. The IR Emission Line Profile Method

Our data set contains a number of IR recombination lines of He II. The strong lines observed in our spectra are for transitions involving levels in the range 6 to 16. Assuming pure recombination lines and accounting for free-free opacity, we model the line profiles using standard Sobolev theory in spherical symmetry (e.g., Mihalas 1978). The total emergent intensity arriving at the Earth along a ray at  $p$  (see Fig. 1) is

$$I_\nu^{\text{emer}}(p) = I_{\nu, c}^{\text{emer}} + I_{\nu, l}^{\text{emer}} \quad (11)$$

where the first term on the RHS is the emergent intensity of the underlying continuum emission and the second term is the emergent intensity of line emission. Both the line and continuum emission

are computed at each frequency in the line profile. In Sobolev theory, the line emission at a given frequency arises from an “isovelocity zone”, which is a region of constant Doppler shift in the flow as perceived by the observer. Figure 1 shows an example of an isovelocity surface. The continuum emission, however, is determined by a volume integral over the whole envelope. The continuous opacity can attenuate the line emission; moreover, the line opacity can diminish the net continuum emission.

It is convenient to define four optical depths. The first three are for the continuous opacity:  $\tau_{\text{fore}}$ ,  $\tau_{\text{aft}}$ , and  $\tau_{\text{tot}}$ . Of these the first is the optical depth that attenuates the line emission (i.e., by matter that lies on the near side of the isovelocity zone with respect to the observer). The second does not (i.e., matter on the rear side of the isovelocity zone). The third is simply the sum,  $\tau_{\text{tot}} = \tau_{\text{fore}} + \tau_{\text{aft}}$ . The fourth optical depth is the Sobolev optical depth  $\tau_S$  associated with the line opacity. This is given by

$$\tau_S = \frac{\kappa_l \rho \lambda}{|dv_z/dz|} = \tau_l \left[ x^4 w^2(x) \frac{dw_z}{dz} \right]^{-1} \quad (12)$$

where the line-of-sight velocity gradient is

$$\frac{dw_z}{dz} = \mu^2 \frac{dw}{dx} + (1 - \mu^2) \frac{w}{x}, \quad (13)$$

where  $\mu = \cos \theta$ , and the scale constant  $\tau_l$  is

$$\tau_l = \frac{\kappa_l \rho_0 \lambda R_*}{v_\infty}. \quad (14)$$

Using these optical depth definitions, the emergent continuum and line intensities are given respectively by

$$I_{\nu,c} = \int_{\tau_{\text{fore}}}^{\tau_{\text{tot}}} B_\nu(T) e^{-\tau} e^{-\tau_S} d\tau + \int_0^{\tau_{\text{fore}}} B_\nu(T) e^{-\tau} d\tau \quad (15)$$

and

$$I_{\nu,l} = S_{\nu,l} (1 - e^{-\tau_S}) e^{-\tau_{\text{fore}}}. \quad (16)$$

If we assume that the wind is isothermal, or at least approximately constant over the radii giving rise to the bulk of the line and continuum emission, the intensity for the continuum reduces to

$$I_{\nu,c} = B_\nu(T_w) (e^{-\tau_{\text{fore}}} - e^{-\tau_{\text{tot}}}) e^{-\tau_S} + B_\nu(T_w) (1 - e^{-\tau_{\text{fore}}}), \quad (17)$$

for  $T_w$  the wind temperature. If the further assumption is made that the departure coefficients for the upper level populations are nearly unity, one has that  $S_{\nu,l} = B_\nu(T_w)$ , and the total emergent intensity for line and continuum emission, including the relevant absorptions, along a ray at  $p$  compactly reduces to

$$I_\nu(p) = B_\nu(T_w) \left[ 1 - e^{-(\tau_{\text{tot}} + \tau_S)} \right] \quad (18)$$

Clearly, outside the line frequencies, the calculation for the continuum emission is given by the same expression only with  $\tau_S = 0$ . We ignore any bound-free contribution to the opacity (see the discussion of §4), but note that the bound-free emissivity at IR wavelengths also scales as  $\rho^2$  so that the form of equation (18) would continue to hold. Electron scattering is also ignored, but it becomes more important at shorter wavelengths where the free-free opacity is smaller. Equation (18) implies that in the line, the intensity is always less than that in the neighboring continuum. In such a case the only way that a line will appear in emission is if the integration of the intensity over the apparent disk of the envelope is larger at line wavelengths. Thus an emission line profile provides us with information about the velocity distribution somewhat beyond the radii at which the neighboring continuum is formed.

We are interested in using the line data to learn about the wind velocity distribution. Figure 3 shows the emergent flux of line emission, given by  $j_\nu \exp(-\tau_{\nu,\text{ff}}) dV$ , for  $j_\nu$  the line emissivity and  $dV$  a differential volume element, along the line-of-sight toward the center of the star. The upper panel is a plot against continuum optical depth, and the lower is against the normalized wind velocity. The two solid curves at top are for explicitly optically thin lines, contrasting the constant expansion-velocity case with  $\beta = 0$  against the  $\beta = 1$  case. Also plotted is a dotted line for an optically thick line with  $\beta = 1$ . From Figure 3, we may conclude that the bulk of the line emission emerges exterior to the radius where  $\tau_{\nu,\text{ff}} = 1$ . In the bottom panel, only the thin (solid) and thick (dotted) line cases for  $\beta = 1$  are shown, since there is no variation of  $v$  with  $r$  for  $\beta = 0$ . We see that

the line emission originates from a fairly broad range of physical wind velocities. At longer wavelengths, where the free-free opacity is larger, the peak of the flux contribution will move to higher wind velocities resulting in emission lines of increasing breadth.

To obtain the total line flux at a given line frequency (or velocity shift  $v = v_z$ ) requires an integration over impact parameter for the corresponding isovelocity zone, as given by

$$f_\nu = \frac{2\pi R_*^2}{d^2} \int_{w_z} I_\nu(p) p dp, \quad (19)$$

where  $d$  is the distance to the star. For thin lines the integrand of equation (19) scales with  $\rho^2 r^2 \exp(-\tau_{\nu,\text{ff}}) \propto x^{-2} w^{-2} \exp(-\tau_{\nu,\text{ff}})$ . The width of the line profile depends on the wind expansion in the region where the line forms. Since there is a finite range of radii that primarily contribute to the line emission, the overall width of the line is set by the velocity at the radius where  $\tau_{\text{ff}} \approx 1$ . Line emission from smaller radii is strongly absorbed, and that from larger radii is small owing to the diminishing emission measure.

In this discussion of the line radiative transfer, the forward approach has been emphasized. As was the case for the continuum, it is possible to use an inverse approach to analyze emission lines, if certain simplifying assumptions hold. The inverse approach can allow one to directly determine the wind velocity law (Cannon 1974; Brown *et al.* 1997; Ignace *et al.* 1998ab). The primary assumptions are that the lines be optically thin, the wind be spherically symmetric, and that there be a relatively distinct photospheric radius. Unfortunately, consideration of the S/N, difficulties with line blends, non-thermal broadening (e.g., from wind instabilities), and the radial extension of the free-free continuum formation zone, have led us to conclude that the application of these inverse techniques to the observed He II profile shapes in WR 136 will not be useful. The method of Ignace *et al.* (1998b) appears to show some promise. It uses the distribution of total line intensities for several thin lines, and the total emission for each line depends on the emission measure. Thus some of the effects that severely bias the inversion of line profile shapes are averaged out. However, there are not enough suitable lines in our dataset to at-

tempt this inversion.

Returning to the forward approach, a key point in modeling the IR spectrum of dense winds is that both the line and continuum optical depths scale with the square of the density. The assumption that the source function for the line and continuum are the same ensures that there is no net absorption feature in the profile. So the situation results in rather symmetric emission profiles, which initially is somewhat counterintuitive, since the absorption of line emission by the continuous opacity varies strongly from the near side of the star (corresponding to blueshifted line frequencies) to the far side (for redshifted line frequencies).

A counter example is provided by wind X-ray emission lines that are expected to be asymmetric in the standard paradigm of distributed wind shocks (Ignace 2001; Owocki & Cohen 2001; Ignace & Gayley 2002). For X-ray lines, the emissivity scales with  $\rho^2$ , and the line emission suffers photo-absorption by the dominant “cool” wind component. Asymmetry in the profile shape results because the continuous opacity makes no contribution to the emission, and such asymmetric morphologies are observed in the *Chandra* spectra of  $\zeta$  Pup (Cassinelli *et al.* 2001). Indeed in the case at hand, we have examined the line emission contribution alone (i.e., with attenuation by free-free absorption) and find it to be strongly asymmetric with blueshifted peak emission, just like the theoretical X-ray lines. However, the absorption of the continuum is also asymmetric, with greatest absorption occurring at blueshifted frequencies. This is why the net profile recovers a fairly symmetric appearance.

To show profile effects explicitly, an analytic expression for the profile shape can be derived in the case of a constant expansion-velocity flow, if the free-free optical depth is quite large. In fact, the profile shape in this limit has previously been derived by Hillier *et al.* (1983), but the result appears there as an unnumbered equation (between their eqs. [13] and [14]), and examples of the profile shapes are not shown. Those authors were more concerned with line equivalent widths. (In their appendix a derivation for the equivalent width is presented for a wind in homologous expansion, with  $v \propto r$ .) The solution for this special case is particularly apt to the problem at hand, so we provide details for the line profile derivation in the

appendix. Results are shown in Figure 4, where a sequence of line profiles are plotted as the ratio of line to continuum optical depth scales,  $\tau_l/\tau_c$ , is varied. The profile is rather “bubble-shaped” and is identically symmetric. Of course, relaxing any of our assumptions will, in general, allow the profiles to develop asymmetries; however, the bubble-shape profiles illustrated by the constant expansion-velocity case are similar to those actually observed in WR 136, as we describe next.

### 3. ISO OBSERVATIONS OF WR 136

We have obtained *ISO* observations of the prototype WN6 Wolf-Rayet star WR 136 (HD 192163). As a member of the Cyg OB1 association, the distance to this star is well-determined ( $d = 1,820$  pc; Lundström & Stenholm 1984). WR 136 is unusual among WN6 stars in that it has a substantial abundance of hydrogen,  $\sim 12\%$  by mass (Crowther & Smith 1996; Hamann *et al.* 1994). Line and continuum spectra of WR 136 were obtained with the SWS spectrometers aboard the *ISO* satellite as described in Table 1. Automated preliminary processing of the data was done using version 7 of the standard pipeline package (OLP-7), and subsequent processing was done as described in detail in Paper I. In this section we present the continuum slopes and line profile widths that can be used to derive density and velocity information for the wind of the star.

#### 3.1. The Continuum Flux Distribution

Continuum measurements were made over the range of 2.8 to 10 microns, beyond which the S/N ratio was insufficient to reliably determine a continuum. The spectrum obtained with the SWS01 spectrometer is displayed in Figure 5, and this has been dereddened using the algorithm of Whittet (1992), with values for  $A_V$  and  $E_{B-V}$  given by van der Hucht (2001). A power-law fit was made to the continuous flux distribution, as shown in Figure 6, that yields a power-law index of

$$\gamma_F = \frac{d \log f_\lambda}{d \log \lambda} = -2.87. \quad (20)$$

This value is to be compared with a slope of  $-2.6$  expected from a constant expansion wind at long wavelengths (Wright & Barlow 1975). The steeper

observed value suggests that either the wind is accelerating, the temperature is varying, or both. However, we find that the power law is somewhat weakly constrained, especially by the low quality data at longer wavelengths. The  $1\sigma$ -confidence interval for acceptable power-law indices is quite asymmetric, with a range of  $-2.75$  to  $-2.9$  that applies to the better quality short wavelength spectrum (the  $-2.87$  is the minimum  $\chi^2$  value). This range is consistent with spectral indices reported by Nugis, Crowther, & Willis (1998), who quote a value of  $-2.75 \pm 0.02$  in the range of 12  $\mu\text{m}$  to 6 cm, and a value of  $-3.15 \pm 0.35$  in the range of 12–25  $\mu\text{m}$ .

Using the range of power laws from our *ISO* data, we can estimate the density variation over the range of radii in which the continuum forms for these wavelengths. In the power-law approach of Cassinelli & Hartmann (1977) described in §2.1, the  $s$  in equation (10) is related to  $\gamma_F$  via  $s = \gamma_F + 1$ , which in our case ranges from  $-1.75$  to  $-1.9$ . Assuming an isothermal wind with  $m = 0$ , the density power law is found to be  $q = (s + 7)/(2s + 6)$ , which ranges from 2.1 to 2.3. But of course, if  $\rho \propto r^{-q}$ , and  $\rho \propto r^{-2}v^{-1}$ , then  $v \propto r^{q-2}$ , which in this case results in  $v \approx r^{0.2}$ . This is a fairly shallow slope, and consequently the continuum data, based on this crude analysis, is likely arising from rather far out in the wind acceleration zone, where the wind is starting to approach constant expansion-velocity.

In terms of a standard wind  $\beta$  law like equation (6), one can make a further identification. Assuming large radius with  $r \gg R_*$ , the velocity gradient is  $d \ln v / d \ln r \approx \beta b R_*/r$ . With  $v \propto r^{0.2}$ , we have that  $\beta \approx 0.2r/bR_*$ , which implies that  $v \approx v_\infty(1 - \beta b R_*/r) \approx 0.8v_\infty$  regardless of the  $\beta$ -exponent. This exercise suggests that our data probe mainly the outer wind acceleration.

#### 3.2. The He II Line Profiles

The high resolution SWS06 observing mode was used to obtain recombination line data with resolving powers ranging from  $\lambda/\Delta\lambda \approx 1300$  to 2500 over wavelengths of 2.8 to 5.0 microns, respectively. We use the seven best He II recombination lines in our study. Figure 7 shows the six lines used for determining the line half-widths (the seventh, 14–11 is too noisy to obtain a reliable width, but is adequate for determining an equivalent width).



Line identifications with comments are given in Table 2. Atomic data and measurements for these lines are provided in Table 3. The HWHMs for the lines are around  $1000 \text{ km s}^{-1}$ , and the instrumental broadening is about  $100 \text{ km s}^{-1}$ . Since the emission profiles are somewhat Gaussian, estimating the effect of instrumental “smearing” is relatively straightforward. The convolution of two Gaussians yields another Gaussian. The width of the resultant Gaussian is given by the rms of the widths for the two input Gaussians, in this case the emission line and the instrumental smearing. Thus, instrumental broadening affects our HWHM determinations at about the 1% level, and so we have ignored it.

Using the line width data, we can make another estimate of the wind velocity law in WR 136. HWHM values were measured for the *red* wing of the six He II recombination lines and are plotted against wavelength in Figure 8. (HWHMs measured from the blue wing are systematically less by about  $100 \text{ km s}^{-1}$ , which we attribute to the influence of line absorption.) A power-law fit was made to this data, yielding a power-law index of

$$\gamma_v = \frac{d \log \text{HWHM}}{d \log \lambda} = 0.22 \pm 0.07, \quad (21)$$

To infer information about  $v(r)$ , a power-law index slope in radius is needed. For this, one could assume that the line emission originates from the vicinity of the pseudo-photosphere of the continuum (i.e., around  $\tau_{\nu, \text{ff}} = 1$ ), since the line emission interior to this region will be strongly absorbed. But without knowing the wind velocity law *a priori*, it is impossible to compute the radius of optical depth unity in the free-free opacity. We can at least estimate the wavelength dependence of the radius as follows.

From the observed continuum emission, we can define the surface equivalent radius that would provide the observed flux, with

$$R_{\lambda, \text{surf}} = d \sqrt{\frac{f_\lambda}{\pi B_\lambda}}. \quad (22)$$

Already from §2.1, we have argued that this radius  $R_{\lambda, \text{surf}}$  will be larger than the radius where  $\tau_{\nu, \text{ff}} = 1$ . Even so, the overall wavelength dependence of  $R_{\lambda, \text{surf}}$  should roughly mimic that of the radius of optical depth unity, namely that at

longer wavelengths, the two radii will increase in size in a manner that is roughly proportional.

With  $f_\lambda$  and  $B_\lambda$  taken as known, the run of  $R_{\lambda, \text{surf}}$  with wavelength can be determined, and we find that  $\gamma_R = d \log R_\lambda / d \log \lambda = 2 + 0.5\gamma_F$  or about 0.6. So we may infer that  $d \log v / d \log R_{\lambda, \text{surf}} = \gamma_v / \gamma_R \approx 0.4$ , which is consistent with the estimate (of 0.2) derived from §3.1 based purely on the continuum slope data. Of course, these two approaches (continuum slope and line width) are not entirely independent, since  $\gamma_R$  is related to  $\gamma_F$ . Nevertheless, the line-width data is independent, and so the consistent results support the argument that we are observing the outer wind acceleration at these wavelengths.

### 3.3. Combined Analysis of Continuum and Lines

We have written a code to compute both free-free emission and recombination line profiles using the formalism of §2.2. We use this code to reproduce the continuum fluxes and line profile shapes for our best He II lines. The goal is to simultaneously constrain the velocity law  $\beta$ , the characteristic wind temperature  $T_w$ , and the wind clumping.

#### 3.3.1. Clumping Factor Effects

Clumpiness, now a well-recognized attribute of many WR stars (e.g., Moffat *et al.* 1988; Hillier 1991; Nugis, Crowther, & Willis 1998; Hamann & Koesterke 1998), is included in our modeling. We define the clumping factor parameter as

$$\langle \rho^2 \rangle = D_c \langle \rho \rangle^2. \quad (23)$$

The wind clumping is assumed to occur on small scales, so as to produce the same emission measure as a smooth wind but with a smaller  $\dot{M}$ . The clumping may occur on a range of scales, but for our theoretical approach, these scales must be small enough that the Sobolev approximation is not invalidated. In essence, this means that the radiative transfer may still be described by integral expressions, in contrast to discrete sums (Hamann & Koesterke 1998b).

#### 3.3.2. Assumed Wind Parameters

We consider the terminal speed to be known from Paper I, at  $v_\infty = 1490 \text{ km s}^{-1}$ . For the mass-

loss rate, Table 4 lists several values for WR 136 as taken from the literature; the method of evaluation; and whether the estimates assumed smooth or clumpy winds. The first four values assumed an underlying smooth wind. For the last value, Nugis *et al.* (1998) used radio observations to derive  $\dot{M}$  values using a clumped wind model, and found that at the large radii where the radio emission is produced, the wind of WR 136 is consistent with no clumping (i.e.,  $D_c \approx 1$ ). On the other hand, Crowther & Smith (1996) conclude in favor of clumping in the wind of WR 136 because otherwise their models overestimate the electron scattering wings of strong optical/NIR lines. That these two different methods yield different clumping predictions must reflect on the fact that the methods sample different radial locations in the wind. It may not be surprising that clumping can be a function of radius (e.g., as in the theoretical models of Runacres & Owocki 2002), and at least for WR 136, the degree of clumping seems to diminish in going from the inner wind to the outer wind.

It is not our goal in this study to determine the mass-loss rate; instead, the unclumped mass-loss rate from Nugis *et al.* is adopted. To study the influence of clumping for the IR continuum and line formation, we assume that the clumping factor is constant over the radii in which these emission form. Our model fits to the observations can thus place constraints on  $D_c$ .

Also needed for our models is a value of the “stellar radius”,  $R_*$ . For other classes of stars, this would typically be the radius of the wind base. For example in the case of Of and OB stars, it is possible to observe a photospheric radiation field from which one can derive basic quantities associated with a “hydrostatic atmosphere”, such as the stellar rotation speed, surface gravity, and effective temperature. Consequently, there is a well-defined radius associated with the wavelength at which a hot star exhibits peak emission (i.e., in the UV/EUV). The only free parameters in the canonical  $\beta$  velocity law equation (1) are the value of  $\beta$  itself and the terminal velocity  $v_\infty$ . The latter is generally determined from the strong and saturated P-Cygni lines in the UV (e.g., Prinja, Barlow, & Howarth 1990) or the widths of forbidden lines.

However, the situation is different for WR stars,

fundamentally because the base of the wind is not observed at any wavelength (Abbott & Conti 1987). The mass-loss rates are so high for the WR stars that the winds are optically thick at all wavelengths. This gives rise to the well-known problem that for such stars, the meaning of stellar radius and effective temperature are ambiguous (e.g., Castor 1970; Cassinelli 1971). There have been two approaches to finding values to use for  $R_*$  and  $T_{\text{eff}}$  in WR stars. One is that model atmospheres are computed that have thick winds (e.g., Hamann & Koesterke 1998ab). The stellar radius is chosen to be at the depth at which the Rosseland mean optical depth reaches a value of 20. Using this radius and the stellar luminosity, a stellar temperature  $T_*$  is defined from the Stefan-Boltzmann relation. The values for WR 136 derived in this way are  $T_* = 70800$  K and  $R_* = 7.5R_\odot$  (Hamann & Koesterke 1998a).

Nugis & Lamers (2000) use another approach based on the idea that there must be a definable hydrostatic star at the base of the wind. These authors start with an estimate of the radius  $R_{\text{evol}}$  of WR stars provided by stellar evolution modeling. For example, using formulae derived by Schaerer & Maeder (1992) for H-deficient stars, Nugis & Lamers find for WR 136,  $R_{\text{evol}} = 1.2R_\odot$  and  $T_{\text{evol}} = 140600$  K. Their radius is  $1/6^{\text{th}}$  as large and their temperature 2 times larger than values derived with the wind modeling approach. Since WR 136 is not completely H-deficient, the radius derived from the evolution models is probably underestimated; however, it should still be smaller than that from the wind-modeling method above.

While the  $R_{\text{evol}}$  approach may provide a good estimate of the underlying size of the star, there is a problem in that the optical depth through the wind to the central star is extremely large, orders of magnitude greater than unity. Given that the radiation field is not strongly peaked in the outward direction deep in the wind, we expect that the rate of increase of the outflow speed is likely to be shallow just above  $R_{\text{evol}}$ . Hence, we do not consider it likely that this evolutionary radius is the proper one to use in a  $\beta$ -law distribution that describes the conditions in the IR line and continuum formation regions of the wind. In other words a velocity law prescription governed by a single value for  $\beta$  is inadequate for describing both the slowly

accelerating inner wind and that in the outer wind. Nevertheless, it is convenient to use the  $\beta$ -law formula to discuss the outer part of the wind that we can probe with our data. Thus the  $bR$  product that appears in the velocity law, would not in this case correspond to the evolutionary radius of the star, nor would the velocity,  $v_0$  necessarily be the sound speed at that radius, but are simply parameters that complete the description of the outer velocity law.

To bring closure to our models, we choose to adopt the value  $R_* = 5R_\odot$  from the wind modeling of WR 136 by Crowther & Smith (1996). Their model is also useful for limiting the possible range in wind temperature. For WR 136, Crowther & Smith (1996) find an effective temperature of 27700 K at a Rosseland optical depth of 2/3, but a “stellar” temperature of 57700 K at an optical depth of 20 corresponding to a stellar radius of  $R_* = 5R_\odot$ . In modeling the forbidden lines at very large radius (100’s of  $R_*$ ), an electron temperature of 13000 K is used (e.g., in Paper I). Recent models of WR winds show variations in  $T_w$  with radius, with  $T_w$  being large at the inner wind, then decreasing with radius to achieve an asymptotic value (e.g., Dessart *et al.* 2000 and Herald *et al.* 2001). In this paper we are attempting to extract information from the ISO observations about the velocity distribution without doing full radiatively-driven hydrodynamic simulations that might ultimately be required. It is likely that the insight developed from this empirical analysis will provide guidance to more detailed studies. So as in Hillier (1987ab), we take the wind to be isothermal in the IR formation region of interest to us. We take the temperatures 27700 K and 57700 K as reasonable limiting values in our models. The basic stellar and wind parameters used for WR 136 are summarized in Table 5.

### 3.3.3. The Fit to the Continuum

For the continuum emission in the vicinity of our line measurements, we have computed a grid of solutions which are shown in Figure 9. There are two sets of plots: one for  $T_w = 27700$  K and one for 57700 K. The three different curves shown as solid in the figure are for  $\beta = 1, 3,$  and 10 (from left to right). The different points are for different clumping factors, with  $D_c = 1, 3, 10, 20,$  and 50, such that  $D_c = 1$  is the lowest point on each curve.

The horizontal and vertical dotted lines demarcate “allowed zones” from the observations, representing the  $1\sigma$  confidence range of models permitted by the errors in the measurements. For the power-law fits to the continuum slope, we use the form  $f_\lambda = f_0 (\lambda/\lambda_0)^p$ , with  $\lambda_0 = 1$  micron. As quoted previously, values of  $p$  range from  $-2.75$  to about  $-2.9$ , with  $-2.87$  giving the minimum  $\chi^2$  fit. The absolute flux error for ISO is about 15%, and propagating errors for the variation in  $p$  results in the allowed range for the flux scale. Favored models are those that match both the observed continuum slope (plotted as the abscissa) and the overall flux scale (plotted as the ordinate), and fall within the indicated error box. Note that we do not actually observe the spectrum at  $1 \mu\text{m}$ ; rather the  $1 \mu\text{m}$  flux level  $f_0$  is a back-extrapolated fiducial value based on the power-law fit to the spectrum.

For comparison we also show models in which the He ionization changes from He III to He II at a radius of  $r = 30R_*$  (the dashed line curves). We chose this radius for the change in ionization on the basis of model calculations by Hillier (1987a) for the well studied WN 4 star WR 6. There are probably differences that will arise by the fact that WR 136 is a WN 6 star instead of WN 4, and because of the fact that WR 136 is not hydrogen free. However, we want to investigate the possible effects of the ionization change and find that Hillier’s study is the best currently available guide. The location of the ionization transition requires the detailed models to provide, for example, the ionizing EUV flux that penetrates through the wind. We suspect that the radius of the ionization transition in WR 136 must be relatively large, because we observe such strong He II recombination lines.

The effect of an ionization change is to shift the curves of Figure 9 primarily in a lateral fashion, and more so for the lower temperature models than for the higher temperature ones. These new curves would alter conclusions as to the velocity law. However we note that rather low clumping factors are still required in the fit shown in the figure. Clearly, low clumping factors are found both with and without the ionization transition. To investigate the other effects that influence the velocity law diagnostics, we shall assume for the remainder of the paper that the wind is fully doubly ionized He.

Focusing on the solid lines of Figure 9, the observed continuum flux data favor a  $\beta$ -value of about 5 for the cooler wind, and 3 for the hotter wind. These values are larger than the value  $\beta = 1$  commonly assumed in WR wind models. However, values as low as  $\beta = 1$  are not strongly ruled out in Figure 9. The influence of the temperature can be understood as follows. A lower temperature reduces the free-free source function, but increases the free-free opacity. For a wind that is isothermal and in constant expansion, as applies to the radio emission, the temperature dependence exactly cancels out (Cassinelli & MacGregor 1986). This cancellation is no longer the case in the accelerating portion of the wind. Also, the effect of the wind acceleration is to modify the density distribution. In the net a larger  $\beta$  both elevates and steepens the density distribution. Increasing  $\beta$  thus leads to a brighter continuum level with a steeper power-law slope.

Consider the effect of changing the clumping factor. An increase in the clumping factor raises the flux level. However for a *fixed*  $\beta$ , the enhanced clumping elevates the density such that the observed continuum emission forms at larger radius and higher speed flow. Consequently, the continuum slope is actually reduced, since the continuum forms in a region closer to constant expansion. Thus to match both the fiducial flux level and the continuum slope, larger  $\beta$ -values are needed for winds of lower temperature.

Note that in the lower temperature case, the power-law slope can actually fall below the canonical 0.6 value of Wright & Barlow (1975) for a constant expansion-velocity wind. This occurs for two reasons: (a) both  $T_w$  and  $\lambda$  are sufficiently low that the Planck function is not entirely in the Rayleigh-Jeans limit, which influences the slope, and (b) the wavelength dependence of the Gaunt factor in the IR band is slightly different from that in the radio band. For the IR free-free Gaunt factor, we use data from Waters & Lamers (1984). These authors computed Gaunt factors down to  $10\mu\text{m}$  only; however, we adopt their expressions for the shorter wavelengths of interest with  $\text{He}^{++}$  as the dominant contribution (with He mass fraction  $Y = 8/9$ ). We also include free-bound opacity from  $\text{H}^+$  and  $\text{He}^{++}$ , again using the Waters & Lamers expressions. The free-bound opacity from the IR and longward has the same scaling

as the free-free, and so the effective Gaunt factor becomes  $g_\nu = g_{\text{ff}} + b_{\text{fb}}$ , where  $b_{\text{fb}}$  is generally much smaller than  $g_{\text{ff}}$ .

### 3.3.4. Fits to the Line Profile Data

To further constrain wind parameters, we have also produced model line profiles to be compared with the observations. To model the lines with the influence of wind acceleration, we again assume that  $\text{He}^{++}$  is the dominant ionization state and calculate the populations of the upper  $\text{He}^+$  levels by assuming LTE with the continuum. The NLTE departure coefficients  $b_k$  for the upper levels of interest ( $k \geq 7$ ) are expected to be near unity (e.g., Storey & Hummer 1995). A grid of line profile calculations are shown in Figure 10, with variations in  $\beta$ , line optical depth  $\tau_l$ , and the wind temperature  $T_w$ . Although these parameters are not truly independent – for example,  $\tau_l$  will depend on both  $\beta$  and  $T_w$ , they are treated as independent for the purpose of indicating the range of profile shapes that can result. The “canonical” model to be used as a reference in this figure (shown as dashed) is for  $\beta = 1$ ,  $D_c = 1$ ,  $T_w = 30000$  K, and  $\tau_l = 1$ . Variation of  $D_c$  is not explicitly shown, but its influence is similar to temperature, in the sense that increasing the clumping or decreasing the wind temperature both result in overall weaker emission lines relative to the continuum level. Note that in our line modeling, we take the inner wind density to be fixed, with  $\rho(R_*) = \dot{M}/4\pi R_*^2 v_0$  a constant. This means that as  $\beta$  is varied,  $b$  also changes to keep  $v_0$  fixed, with  $v_0 = 0.0075v_\infty$ .

Before applying the line fits to the data, we first demonstrate that the observed lines are sampling part of the wind acceleration by overplotting the asymptotic expression for emission line profiles with the observations in Figure 11 (see Eq. [A15]). For our seven best lines, the emission profile shapes from a wind expanding at the terminal speed are consistently too broad, and so the line formation must occur in the lower velocity, accelerating portion of the flow.

In fitting the observed profiles, both  $\beta$  and  $D_c$  are allowed to vary; however, we must also allow for *additional* broadening to approximate the influence of “turbulence” in the wind, and so a “broadening parameter”  $\sigma$  is introduced. This additional broadening is motivated by the commonly held fact that the winds of hot stars are

structured. The velocity distributions of hot star winds are non-monotonic, with variations associated with wind shocks that reach outflow speeds that can be significantly greater than the asymptotic value obtained at large radius. Line-driven wind instability effects can produce sharp drops and spikes in the wind velocity and density distribution in O star winds (Lucy & Solomon 1970; Lucy 1982; Owocki, Castor, & Rybicki 1988; Feldmeier *et al.* 1997). Similar effects are theoretically expected for WR winds (Gayley & Owocki 1995), and structure is inferred from UV and optical emission profile variations (e.g., St-Louis *et al.* 1995; Lépine & Moffat 1999). Of specific relevance to this paper, an analysis of the C IV doublets near 1550Å reveal blueshifted black troughs and somewhat larger absorption edge velocities for many classes of hot star winds, including WR stars (Prinja *et al.* 1990). The difference between the trough and edge velocities, amounting to as much as 25% of  $v_\infty$  for WR winds, is commonly interpreted as arising from the wind being structured in velocity. For WR 136, Prinja *et al.* report an edge velocity of 2700 km s<sup>-1</sup> but a terminal speed of 1600 km s<sup>-1</sup>, amounting to a difference of over 1000 km s<sup>-1</sup>. Based on our previous comment about the convolution of Gaussian profile shapes, broadening of this order would increase the line widths of our model profiles by about 40%.

To constrain values of  $\beta$  and  $D_c$  for the IR lines, we have computed a grid of line profiles to fit our best line, He II 7–6, which is strong and has excellent S/N. Using the terminal speed of  $v_\infty=1490$  km s<sup>-1</sup> from Paper I, we compute the required additional broadening from  $\sigma = \sqrt{HWHM_{\text{obs}}^2 - HWHM_{\text{mod}}^2}$ , with results shown in Figure 12, to match the line HW (defined as the line HW in the red wing to be compared with the observed values from Tab. 3). The solid lines are for the hotter wind, and the dashed ones for the cooler wind temperature. In each case, the upper curve is for  $D_c = 1$  and the lower for  $D_c = 3$ . Larger values of  $D_c$  at a fixed  $\beta$  will produce broader line widths resulting in lower  $\sigma$ -values, but the analysis of the continuum emission (based on Fig. 9) rules out  $D_c$  greater than about 3. We did consider the influence of a transition in the He-ionization at  $r = 30R_*$ . With this transition the continuum-normalized line emission drops by about 10% or less, and the shape is not dra-

matically affected. The effect is not major because both the line and free-free opacities are affected so as to be partially compensating when the line is continuum normalized, and so we continue to assume that the wind is pure He III.

In Figure 12, the lower dotted line is the instrumental broadening, representing a minimum threshold for  $\sigma$ . A strong upper limit would be 1200 km s<sup>-1</sup> based on the UV C IV line absorption (not shown in the Figure). Here we have an even better constraint from the fact that the wind cannot have clumping factors below unity. At this point, the lines would suggest that  $\beta$ -values below 1 are probably not consistent with the observed 7–6 line.

However, we can do better than this. Wolf-Rayet stars are sources of X-ray emission (e.g., Pollock 1987; Wessolowski 1996; Ignace, Oskinova, & Foullon 2000). Recent pointed observations of 3 putatively single WR stars by XMM-Newton indicate hot gas of at least a few million Kelvin in the winds (Skinner 2002ab; Ignace, Oskinova, & Brown 2003). If arising from wind shocks, as would be the standard explanation, shock velocity jumps of at least a few hundred km s<sup>-1</sup> would be needed to generate hot gas at these temperatures. A range of 300-500 km s<sup>-1</sup> would seem to be reasonable, and such variations relative to the mean flow would lead to “broadening” of the IR lines. The observed X-rays do not emerge from the same radii as the IR continuum and He II lines; the X-rays emerge mainly from farther out in the wind, but only because of strong photo-absorption by the dense WR wind.

Consequently, we indicate in Figure 12 with a circled asterisk a “best representation” for the wind of WR 136 that takes into account (a) low clumping based on the continuum analysis, (b) the rather broad but finite range of  $\beta$  values from the continuum constraints, and (c) a modest level of  $\sigma$  necessary to account for the fact that WN stars are X-ray sources. The result is  $D_c = 2$ , with  $\beta = 3$  for the cool wind model and  $\beta = 2$  for the hot wind model. Naturally, based on the discussion of the He ionization, and ambiguity regarding the broadening processes intrinsic to the winds of WR stars,  $\beta$  is somewhat loosely constrained, although a clumping factor that is not too large seems required.

Using these preferred values for  $\beta$  and  $D_c$ , Fig-

ures 13 and 14 show the model profiles (dotted) as overplotted on the observed emission lines (solid), for the cool and hot wind cases respectively. Note that the lines in these figures are continuum normalized. A key for the line transitions is provided at bottom center. In addition to broadening processes, line blends may influence some of the observed profiles widths, particularly in the wide He II 16–10 line and the wings of He II 9–7, and the somewhat blueward broadened He II 7–6 line.

Inspection of our model results for the lines also confirms the earlier estimates that the ISO data are not sampling the innermost wind acceleration. Optical depth unity in the free-free opacity occurs at a radius of  $v \gtrsim 0.3v_\infty$  for our shortest wavelength line. Still, our analysis places interesting constraints on the value of  $\beta$  and  $D_c$  for the extended wind acceleration of WR 136.

#### 4. DISCUSSION

We have argued that WR stars should have a significantly different velocity distribution than OB stars, for which the radiation field is more forward-peaked near the base of the wind. The many thick lines and the small mean free paths deep in the star should cause the initial rise in velocity to be gradual. One would expect that a flow which is driven by multi-line scattering would have a large value of  $\beta$ , a conclusion that we have sought to test using IR observations of WR 136 obtained with the ISO satellite. Line and continuum data have been analyzed and are found to be sensitive primarily to the outer part of the wind at the observed wavelengths. Although our ISO data do not probe the deep layers where multi-line scattering processes are most important, the velocity range that is probed is still of interest. If the momentum factor is say 10, then even in going from 0.7 to 1.0 times the terminal speed, multi-line scattering is required of the radiation field seeping through the corresponding wind layers to account for the final acceleration.

We have found that it is possible to obtain a simultaneous fit to both the continuum and the He II recombination lines from the ISO data for WR 136. We made calculations at two different wind temperatures:  $T_w \approx 60000$  K and  $T_w \approx 30000$  K. Low clumping factors with  $D_c$  of 1–3 are found. The wind velocity law is loosely

constrained, but a value of 2–3 appears consistent with the various constraints imposed by the continuum data, the emission line shapes, and the expectation of “turbulent” broadening in the flow arising from wind structure. Our estimate for  $\beta \approx 2$  to 3 falls in the “gradual acceleration” range that is perhaps appropriate for multi-line scattering acceleration.

For comparison a study of emission line profile variability by Lépine & Moffat (1999) included WR 136 as one of their sources. They observed He II 5411 and draw several interesting conclusions. First, they find that the turbulence in the wind of WR 136 is typical of other WN stars in their study. And second, they derive the product  $\beta R_* \approx 75$ . For the radius of the wind base that we have adopted ( $R_* = 5R_\odot$ ), this would imply a  $\beta$  of about 15. However, as the authors point out, as well as Koesterke, Hamann, & Urrutia (2001), exactly how one relates a  $\beta$ -value derived from features observed in Doppler shift space to physical wind velocities is not clear, because there is almost certainly a flow of wind material past the clumps which are continually forming and dissipating in the wind. So although the data of Lépine & Moffat for WR 136 would imply an extensive region of wind acceleration, the  $\beta$  may not describe the ambient wind, nor does the  $R_*$  derived necessarily refer to the base of the wind. Our method is to infer  $\beta$  through the influence of density on the formation of the IR continuum and He II lines. Our results are perhaps complementary to those of Lépine & Moffat, but we are not studying the same phenomenon.

Our derived low level of clumping is also interesting, since it suggests that the large scale wind flow that is sampled by the radio observations and is also claimed to be unclumped (Nugis *et al.* 1998) extends fairly deep into the wind of WR 136 where the IR emission forms. Perhaps clumps that exist deep in a wind can be dissipated by wind drag with the matter blending into the ambient wind.

In future studies, one could attempt to use somewhat shorter near-IR spectral data to sample the wind acceleration at smaller radii; however, this will probably be limited by the fact that high electron optical depths and strong line-blanketing effectively “veil” the innermost wind acceleration zone. Perhaps there is no direct technique for observationally probing the low velocity portion of

the densest WR winds.

We express appreciation to the staff at the ISO center. We are also grateful to Ken Gayley and Henny Lamers for their insightful discussions on this topic, and an anonymous referee for several helpful comments. The ISO Spectral Analysis Package (ISAP) is a joint development by the LWS and SWS Instrument Teams and Data Centers. Contributing institutes are CESR, IAS, IPAC, MPE, RAL and SRON. This research was supported by NASA grants NAG5-3315 and 1207129 (JPL).

### A. Analytic Line Profile Shapes for Constant Expansion Velocity Winds

The emergent intensity  $I_\nu$  at impact parameter  $p$  within the line frequencies will be given by the sum of the line component  $I_{\nu,l}$  and the continuum component  $I_{\nu,c}$ . Adopting Sobolev theory for the line formation, assuming that the line optical depth scales with  $\rho^2$ , and assuming the continuous emission and opacity is free-free, the respective intensities were given in eqs. (16) and (17). Implicit is that the wind is also isothermal. Further assuming that  $S_{\nu,l} = B_\nu$ , the total intensity expression reduces to

$$I_\nu(p) = I_{\nu,l} + I_{\nu,c} = B_\nu \left[ 1 - e^{-(\tau_{\max} + \tau_S)} \right], \quad (\text{A1})$$

which was also given in eq. (18). For rays that intercept the stellar core, the emergent stellar intensity is

$$I_\nu(p) = I_{\nu,*} e^{-(\tau_{\max} + \tau_S)}, \quad (\text{A2})$$

where the Sobolev optical depth  $\tau_S$  is taken to be zero for red-shifted frequencies in the line, since those resonance points all lie aft of the star.

In the case of constant wind expansion, the line profile shape including the influence of the continuous opacity is analytic in a certain limit as we now show. First, the Sobolev optical depth is given by

$$\tau_S = \tau_l x^{-4} w^{-2} \left[ \mu^2 \frac{dw}{dx} + (1 - \mu^2) \frac{w}{x} \right]^{-1}. \quad (\text{A3})$$

For constant expansion-velocity, this reduces to

$$\tau_S = \tau_l x^{-3} (1 - \mu^2) = \tau_l \sin \theta p^{-3}. \quad (\text{A4})$$

where we have used the fact that  $p = x \sin \theta$ . The free-free optical depth is given by

$$\tau_{\text{ff}} = \tau_c \int_z^\infty \frac{dz}{x^4 w^2}. \quad (\text{A5})$$

For constant expansion-velocity, and re-expressing the integral in terms of  $p$  and  $\theta$ , an analytic solution exists giving analytically to yield

$$\tau_{\text{ff}} = \frac{1}{2} \tau_c p^{-3} (\theta - \sin \theta \cos \theta). \quad (\text{A6})$$

The value of  $\tau_{\max}$  in eqs. (A1) and (A2) depends on  $p$  as follows:

$$\tau_{\max} = \begin{cases} \frac{\tau_c}{2p^3} (\theta - \sin \theta \cos \theta) & (p < 1), \\ \frac{\pi}{2} \frac{\tau_c}{p^3} & (p \geq 1) \end{cases} \quad (\text{A7})$$

The observed flux of line emission at any frequency in the line will be

$$\begin{aligned} f_\nu &= 2\pi \frac{R^2}{D^2} \int_{w_z} I_\nu(p) p dp \\ &= 2\pi B_\nu(T_w) \frac{R^2}{D^2} \left\{ \int_0^{p_{\min}} \frac{I_{\nu,*}(T_*)}{B_\nu(T_w)} p dp [1 - \exp(-0.5\tau_c h(\theta) p^{-3})] \right. \\ &\quad + \int_{p_{\min}}^1 \frac{I_{\nu,*}(T_*)}{B_\nu(T_w)} p dp [1 - \exp(-0.5\tau_c h(\theta) p^{-3} - \tau_S \sin \theta p^{-3})] \\ &\quad \left. + \int_1^\infty p dp [1 - \exp(-0.5\pi \tau_c p^{-3} - \tau_S \sin \theta p^{-3})] \right\}, \end{aligned} \quad (\text{A8})$$



where

$$h(\theta) = \theta - \sin \theta \cos \theta. \quad (\text{A10})$$

For blue-shifted frequencies,  $p_{\min} = \sin \theta$  since the isovelocity surfaces are cones of constant opening angle that intercept a spherical core photosphere. Although all of the stellar photosphere suffers absorption via the free-free opacity, only the annulus of the star from  $\theta$  to  $\pi/2$  will be diminished by the line opacity. At red-shifted frequencies,  $p_{\min} = 1$  and the second integral in (A9) vanishes; there is no line emission for  $p < 1$  owing to stellar occultation.

To solve these integrals, we make the change of variable  $u^3 = \tau_c/p^3$ . The integrals become

$$f_\nu = 2\pi \tau_c^{2/3} B_\nu(T_w) \frac{R^2}{D^2} \left\{ \int_{\tau_c^{1/3} p_{\min}^{-1}}^{\infty} u^{-3} du \frac{I_{\nu,*}(T_*)}{B_\nu(T_w)} [1 - \exp(-0.5h(\theta) u^3)] \right. \\ \left. \int_{\tau_c^{1/3}}^{\tau_c^{1/3}/p_{\min}} u^{-3} du \frac{I_{\nu,*}(T_*)}{B_\nu(T_w)} [1 - \exp(-0.5h(\theta) u^3 - \tau_S \tau_c^{-1} \sin \theta u^3)] \right. \\ \left. \int_0^{\tau_c^{1/3}} u^{-3} du [1 - \exp(-0.5\pi u^3 - \tau_S \tau_c^{-1} \sin \theta u^3)] \right\} \quad (\text{A11})$$

$$(\text{A12})$$

It is important to note that the frequency information is contained in the functions of  $\theta$  via  $w_z = -\mu$ , and also that these functions are constants of the integration which is over  $u$ .

There is in fact an analytic solution to this form of integral given in Gradshteyn & Ryzhik (1994; Eq. 3.478, #2), for which the relevant result is

$$\int_0^{\infty} u^{-3} du (1 - e^{-au^3}) = 1.5 \Gamma(4/3) a^{2/3}. \quad (\text{A13})$$

This solution is applicable to the case at hand in the limit that  $\tau_c^{1/3} \gg 1$ , with the result

$$f_\nu = 3\Gamma(4/3) \pi B_\nu(T_w) \tau_c^{2/3} \left( \frac{\pi}{2} + \frac{\tau_l}{\tau_c} \sqrt{1 - w_z^2} \right)^{2/3}. \quad (\text{A14})$$

Interestingly, for a strong line with  $\tau_l \gg \tau_c$ , the profile shape reduces to

$$f_\nu = 3\Gamma(4/3) \pi B_\nu(T_w) \tau_l^{2/3} (1 - w_z^2)^{1/3}. \quad (\text{A15})$$

The results of this derivation show that symmetric emission profiles result, which are overall similar in appearance to those observed for WR 136. The rounded shape of the profiles implies that a measurement of the widths of these lines would seriously underestimate the speed of the wind flow. Examples of the normalized profile shape of eq. (A15) for various values of the ratio  $\tau_l/\tau_c$  are given in Figure 4.

## REFERENCES

- Abbott, D. C., & Conti, P. S. 1987, ARAA, 25, 113
- Abbott, D. C., Torres, A. V., Biegging, J. H., & Churchwell, E. 1986, ApJ, 303, 239
- Auer, L. H., & Koenigsberger, G. 1994, ApJ, 436, 859
- Cannon, C. J. 1974, A&A, 34, 387
- Barlow, M. J., Roche, P. F., & Aitken, D. K. 1988, MNRAS, 232, 821
- Brown, J. C., Richardson, L. L., Cassinelli, J. P., & Ignace, R. 1997, A&A, 325, 677
- Cassinelli, J. P. 1971, ApJ, 165, 265
- Cassinelli, J. P., & Hartmann, L. W. 1977, ApJ, 212, 488
- Cassinelli, J. P., & MacGregor, K. B. 1986, in *Physics of the Sun*, v. 3 (Dordrecht: Reidel), 47
- Cassinelli, J. P., Cohen, D. H., & Sanders W. 1997, in *Understanding X-ray Emission from Early-Type Stars*, Eds H. Tannenbaum, N. White, & P. Sullivan (Cambridge MA, Harvard-Smithsonian), p. 294
- Cassinelli, J. P., Miller, N. A., Waldron, W. L., MacFarlane, J. J., & Cohen, D. H. 2001, ApJ 554, 55
- Castor, J. I. 1970, MNRAS, 149, 111
- Castor, J. I., Abbott, D. C., & Klein, R. I. 1975, ApJ, 195, 157
- Storey, M. 1999, ApJ, 518, 890
- Crowther, P., & Smith, L. J. 1996, A&A, 305, 541
- Dessart, L., Crowther, P. A., Hillier, D. J., Willis, A. J., Morris, P. W., & van der Hucht, K. A. 2000, MNRAS, 315, 407
- Feldmeier, A., Puls, J., & Pauldrach, A. W. A. 1997, A&A, 322, 878
- Friend, D. B., & Abbott, D. C. 1986, ApJ, 311, 701
- Gayley, K. G., & Owocki, S. P. 1995, ApJ, 446, 801
- Gayley, K. G., Owocki, S. P., & Cranmer, S. R. 1995, ApJ, 442, 296
- Gradshteyn, I. S., & Ryzhik, J. M. 1994, *Table of Integrals, Series, and Products*, 5th ed. (Academic Press)
- Groenewegen, M. A. T., Lamers, H. J. G. L. M. 1989, A&A, 79, 359
- Hamann, W.-R., & Koesterke, L. 1998a, A&A, 333, 251
- Hamann, W.-R., & Koesterke, L. 1998b, A&A, 335, 1003
- Hamann, W.-R., & Koesterke, L. 2000, A&A, 360, 647
- Hamann, W.-R., Wessolowski, U., & Koesterke, L. 1994, A&A, 281, 184
- Harries, T. J., Hillier, D. J., & Howarth, I. D. 1999, MNRAS, 302, 499
- Herald, J. E., Schulte-Ladbeck, R. E., Eenens, P. R. J., & Morris, P. 2000, ApJS, 126, 469
- Herald, J. E., Hillier, D. J., & Schulte-Ladbeck, R. E. 2001, ApJ, 548, 932
- Hillier, D. J., Jones, T.J., Hyland, A.R. 1983, ApJ, 271, 221
- Hillier, D. J. 1987, ApJS, 63, 947
- Hillier, D. J. 1987, ApJS, 63, 965
- Hillier, D. J. 1991, in *Stellar Atmospheres: Beyond Classical Models*, NASTO ASI Ser. C., v. 341 (Dordrecht: Kluwer), 317
- Hillier, D. J., & Miller, D. L. 1999, ApJ, 519, 354
- van der Hucht, K. A. 2001, *New Astronomy Reviews*, 45, 135
- Ignace, R. 2001, ApJ, 549, L119
- Ignace, R., Cassinelli, J. P., & Bjorkman, J. E. 1996, ApJ, 505, 910
- Ignace, R., Brown, J. C., Richardson, L. L., & Cassinelli, J. P. 1998a, A&A, 330, 253
- Ignace, R., Brown, J. C., Milne, J. E., & Cassinelli, J. P. 1998b, A&A, 337, 223
- Ignace, R., Oskinova, L. M., & Foullon, C. 2000, MNRAS 318, 214
- Ignace, R., Cassinelli, J. P., Quigley, M. F., & Babler, B. 2001, ApJ, (Paper I)
- Ignace, R., & Gayley, K. G. 2002, ApJ, 568, 954
- Ignace, R., Oskinova, L. M., & Brown, J. C. 2003, ApJ, submitted
- Kuhi, L. V. 1973, ApJ, 180, 783
- Lépine, S., & Moffat, A. F. J. 1999, ApJ, 514, 909

- Lundström, I., & Stenholm, B. 1984, *A&A*, 138, 311
- Lucy, L. B. 1982, *ApJ*, 255, L278
- Lucy, L. B., & Solomon, P. M. 1970, *ApJ*, 159, 879
- Lucy, L. B., & Abbott, D. C. 1993, *ApJ*, 405, 738
- Mihalas, D. 1978, *Stellar Atmospheres*, 2nd ed. (San Francisco: Freeman)
- Milne, E. A. 1926 *MNRAS*, 86, 459
- Moffat, A. F. J., Drissen, L., Lamontagne, R., & Robert, C. 1988, *ApJ*, 334, 1038
- Morris, P. W., van der Hucht, K. A., Crowther, P. A., Hillier, D. J., Dessart, L., Williams, P. M., & Willis, A. J. 2000, *A&A*, 353, 624
- Nugis, T., & Niedzielski, A. 1995, *A&A*, 300, 327
- Nugis, T., Crowther, P. A., & Willis, A. J. 1998, *A&A*, 333, 956
- Nugis, T., & Lamers, H. J. G. L. M. 2000, *A&A*, 360, 227
- Onifer, A. J., & Gayley, K. G. 2003, *ApJ*, 590, 473
- Owocki, S. P., Castor, J. I., & Rybicki, G. B. 1988, *ApJ*, 335, 914
- Owocki, S. P., & Cohen, D. H. 2001, *ApJ*, 559, 1108
- Panagia, N., & Felli, M. 1975, *A&A*, 39, 1
- Pauldrach, A., Puls, J., & Kudritzki, R. P. 1986, *A&A*, 164, 86
- Pollock, A. M. T. 1987, *ApJ*, 320, 283
- Prinja, R. K., Barlow M. J., & Howarth, I. D., 1990 *ApJ*, 361, 607
- Runacres, M. C., & Owocki, S. P. 2002, *A&A*, 381, 1015
- Schaerer, D., & Maeder, A. 1992, *A&A*, 263, 129
- Schulte-Ladbeck, R. E., Eenens, P. R. J., & Davis, K. 1995, *ApJ*, 454, 917
- Schmutz, W. 1997, *A&A*, 321, 268
- Skinner, S. L., Zhekov, S. A., Güdel, M., & Schmutz, W. 2002a, *ApJ*, 572, 477
- Skinner, S. L., Zhekov, S. A., Güdel, M., & Schmutz, W. 2002b, *ApJ*, 579, 764
- Springmann, U.W.E 1994, *A&A*, 289, 505
- St-Louis, N., Dalton, M. J., Marchenko, S. V., Moffat, A. F. J., & Willis, A. J. 1995, *ApJ*, 452, L57
- Storey, P. J., & Hummer, D. G. 1995, *MNRAS*, 272, 41
- Vink, J. S., de Koter, A., & Lamers, H. J. G. L. M. 2000, *A&A*, 362, 295
- Wessolowski, U. 1996, in *Röntgenstrahlung from the Universe*, (eds.) H. Zimmermann, J. Trümper, and H. Yorke, MPE Report 263, 75
- Waters, L. B. F. M., & Lamers, H. J. G. L. M. 1984, *A&AS*, 57, 327
- Whittet, D. C. B. 1992, *Dust in the Interstellar Medium*, IOP Publishing Ltd., 65
- Willis, A. J., Dessart, L., Crowther, P. A., Morris, P. W., Maeder, A., Conti, P. S., & van der Hucht, K. A. 1997, *MNRAS*, 290, 371
- Wright, A. E., & Barlow, M. J., 1975, *MNRAS*, 170, 41

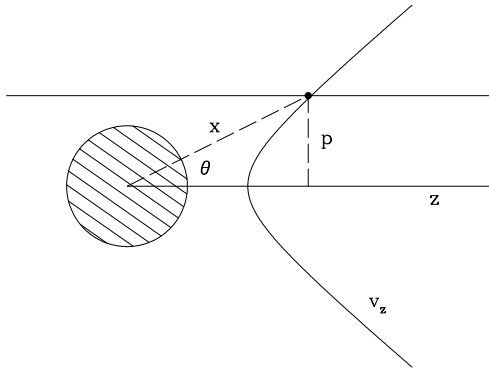


Fig. 1.— The geometry used in our calculations. All lengths are normalized to the stellar radius  $R_*$ . The observer is to the right. The observer coordinates are the cylindrical system  $(p, \alpha, z)$ , with azimuth  $\alpha$  not shown. The star has spherical coordinates  $(r, \theta, \phi)$ . With the assumption of spherical symmetry, we chose  $\theta$  measured from the  $z$ -axis as indicated. Also shown is a contour for an isoveLOCITY zone with  $v_z = \text{constant}$  and a ray passing through the envelope from the observer direction. At the frequency in the line corresponding to the Doppler shift  $v_z$ , the contribution to the observed emission along this ray includes line emission from the indicated point and continuum emission from both fore and aft of this point, along with the associated attenuations.

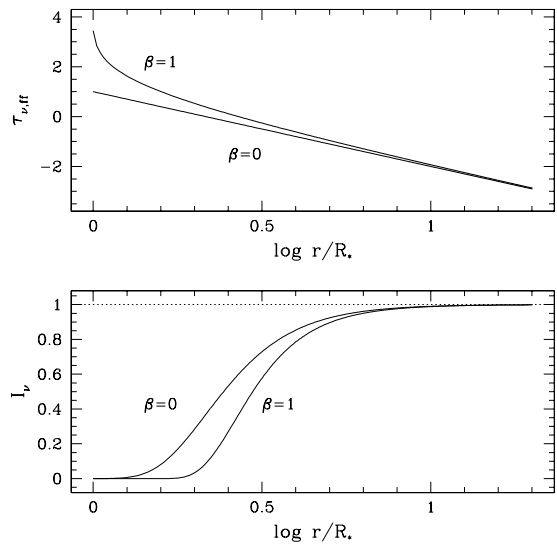


Fig. 2.— Illustrates the influence of the velocity law on the optical depth (top) and emergent intensity (bottom) with  $I_\nu = B_\nu \exp(-\tau_{\nu,\text{ff}})$  along the line-of-sight to the star. The two cases shown are for  $\beta = 0$  (constant expansion-velocity) and  $\beta = 1$ . Unlike a static exponential atmosphere, the extended envelope effects of an expanding wind lead to an attenuation profile that is not especially sharp as a function of radius.

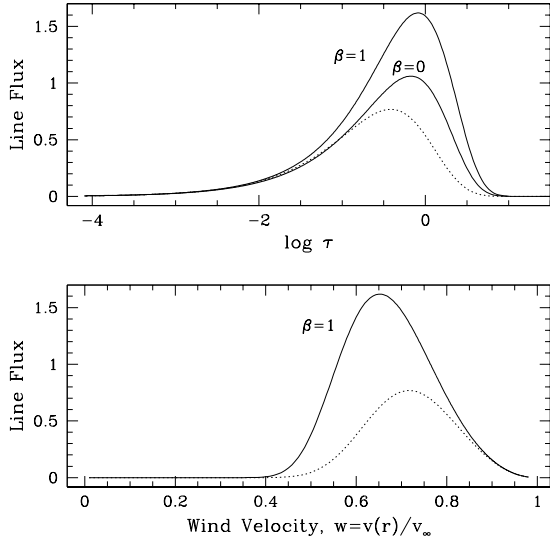


Fig. 3.— Illustrates the influence of the velocity law on the emergent line contribution function along the line-of-sight to the star plotted against the continuum optical depth (top) and wind velocity in the wind (bottom). At top, the two solid curves are optically thin lines for the indicated  $\beta$ -laws. The dotted line is for an optically thick line with  $\beta = 1$ . The effect of large line optical depth is to reduce the amount of emergent line flux and shift the peak location to larger radii. At bottom, just the  $\beta = 1$  curves are plotted against the normalized wind velocity. The range of velocities over which line flux contributions arise is seen to be fairly broad. In this case, for the optically thin line, the peak in the line flux contribution occurs around  $v = 0.65v_\infty$  and has a full width of  $\approx 0.24v_\infty$ .

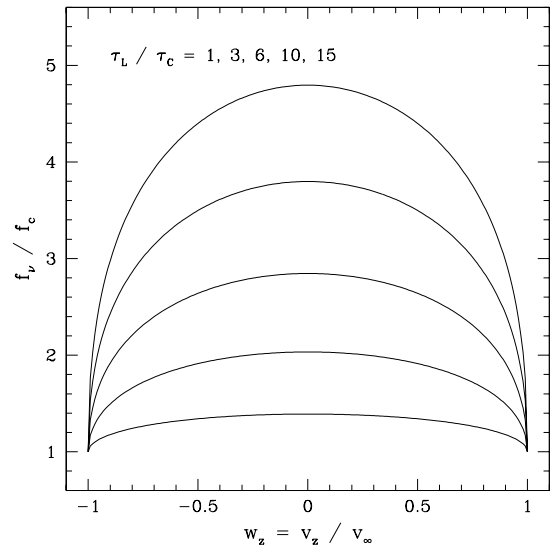


Fig. 4.— A sequence of theoretical emission profiles for a constant expansion-velocity wind as the parameter  $\tau_l/\tau_c$  is varied, where  $\tau_l$  is the scale factor for the line optical depth, and  $\tau_c$  is the scale factor for the free-free optical depth. The profiles are continuum normalized and plotted in velocity units normalized to the wind terminal speed.

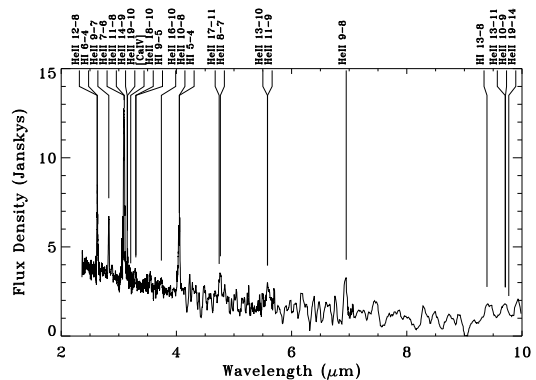


Fig. 5.— The de-reddened low resolution (SWS01) spectrum of WR 136. Major emission features, including the He II recombination lines used in the analysis in this paper are identified. Beyond about  $6 \mu\text{m}$ , the signal-to-noise ratio is seriously degraded, precluding derivation of the velocity law in the outermost regions of the stellar wind.

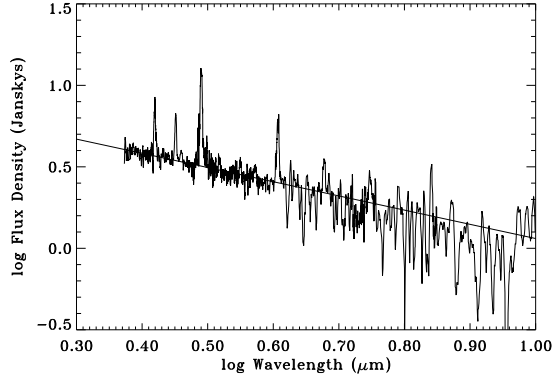


Fig. 6.— The de-reddened continuum flux distribution. This continuum is fit with a power law to give the index,  $\gamma_F = d \log f_\lambda / d \log \lambda = -2.87$ .

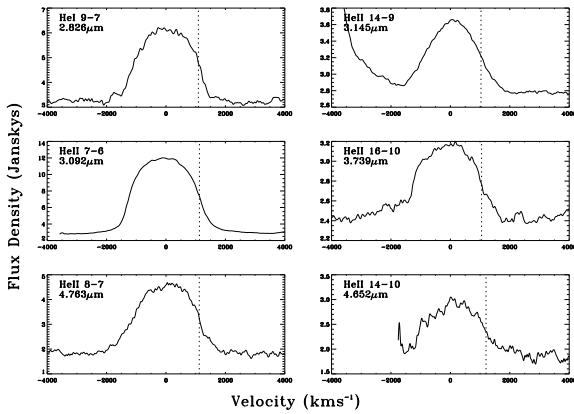


Fig. 7.— High resolution (SWS06) spectra of six He II recombination lines. The spectra have not been de-reddened. With reference to the red wing, the HWHM velocities measured for our analysis are indicated by vertical dashed lines.

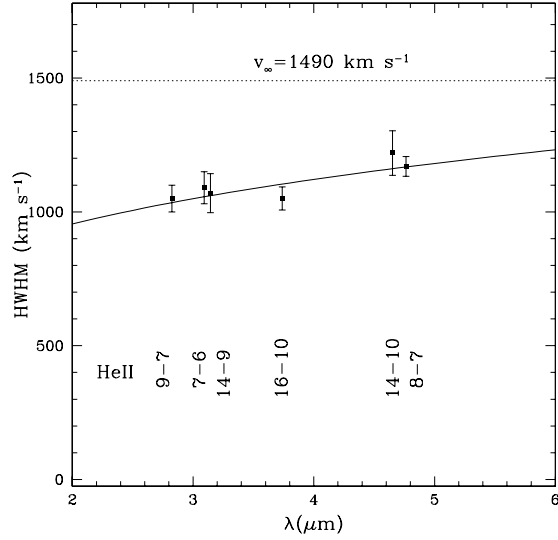


Fig. 8.— Velocity as a function of wavelength as determined by the HWHM of the He II recombination lines. The terminal speed  $v_\infty = 1490 \text{ km s}^{-1}$  is indicated as a dotted horizontal line. The distribution is fit with a power law to give the index,  $\gamma_V = d \log \text{HWHM} / d \log \lambda = 0.22$ .

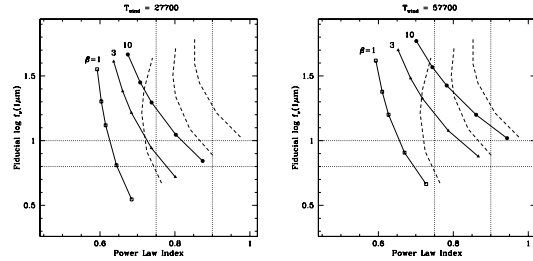


Fig. 9.— Shown as dotted lines are the  $1\sigma$  “allowed” zones from the ISO data. Model calculations for the continuum slope (abscissa) and flux level (ordinate). Left is for a modest wind temperature of 27700 K and right for 57700 K. The three solid curves in each panel are for  $\beta = 1, 3, \text{ and } 10$ . The points are for different clumping factors  $D_c = 1, 3, 10, 20, \text{ and } 50$ , moving from bottom to top. The dashed lines are for models with a transition from He III to He II at  $r = 30R_*$ . Although the curves can shift significantly (especially for lower temperature), the shift is mostly lateral such that low values of  $D_c$  are favored with or without the Helium ionization transition.

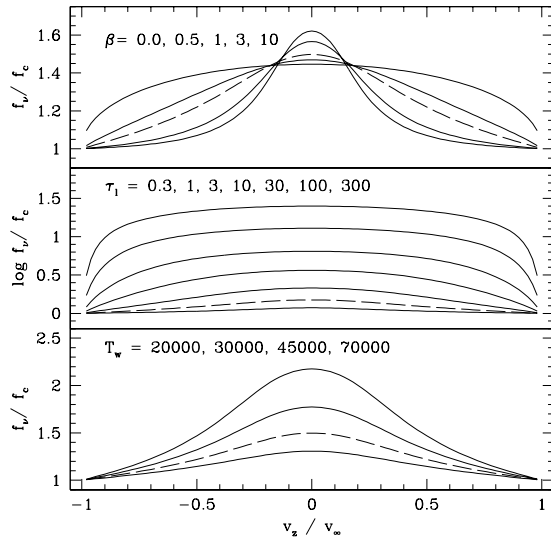


Fig. 10.— A sequence of model emission line profiles to illustrate the effects of varying different parameters. At top, line profile calculations with higher  $\beta$  have narrower half-widths. At middle, line profiles of higher optical depth  $\tau_l$  have stronger emission. At bottom, winds of higher temperature  $T_w$  yield relatively stronger lines. (The same would apply for winds of lower  $D_c$ -values.) The lines are continuum normalized, so one should be aware that the variation of  $\beta$  and  $T_w$  changes the continuum. Even though these parameters are not in fact independent, by varying them independently, we obtain a grid of models to illustrate the range of line widths and strengths that can result.

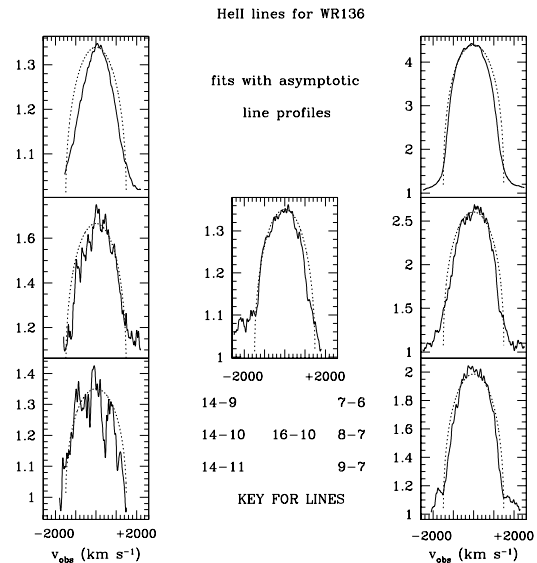


Fig. 11.— Application of the constant expansion-velocity line profile shape to the observed emission lines (plotted as continuum normalized). These theoretical asymptotic forms actually match the observed lines fairly well, although typically being somewhat broader (especially clear in the 14-11 line). Even so, better fits arise when a velocity law is included, especially in light of the fact that there is some blending that likely adds extra broadening to the lines of interest.

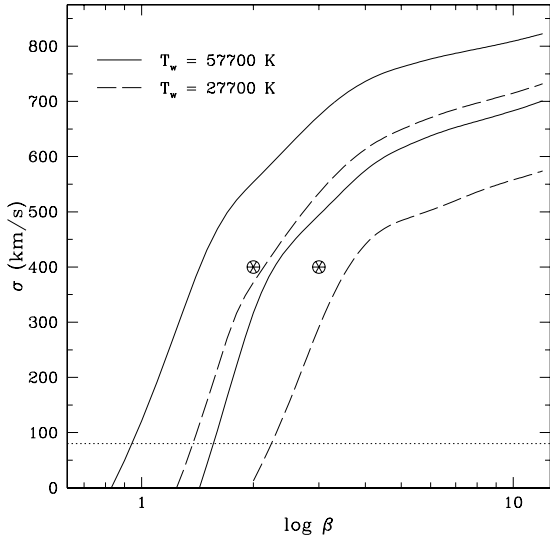


Fig. 12.— A plot of the line broadening  $\sigma$  required to bring model line widths into agreement with that observed in the He II 7–6 line. The solid lines are for  $T_w = 57700$  K and the dashed ones for  $T_w = 27700$  K. In each case the clumping factor  $D_c = 1$  for the upper curve and  $D_c = 3$  for the lower curve. The lower line is the minimum  $\sigma$  set by the instrumental broadening. The two starred points indicate models with  $\beta$ ,  $D_c$ , and  $\sigma$  that meet all the requirements for the data, with the point at left for the higher temperature wind.

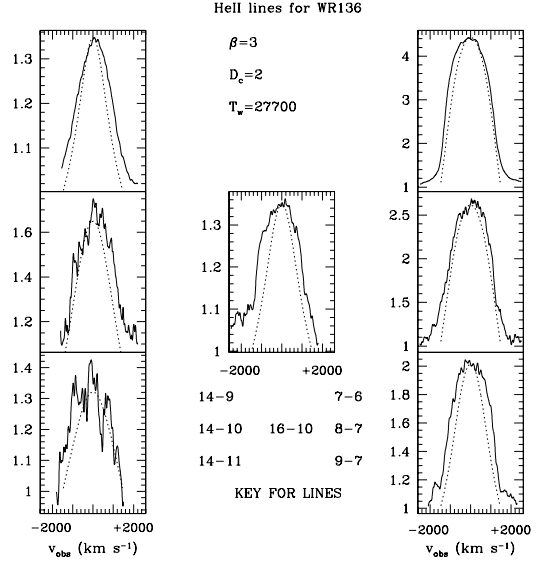


Fig. 13.— Shown as dashed lines are the pre-broadened line models with  $\beta = 3$ ,  $D_c = 2$ , and a wind temperature of  $T_w = 27700$  K overplotted with the observed He II lines.

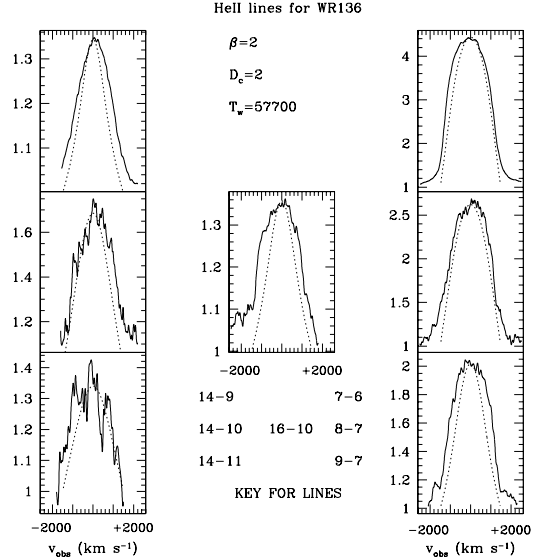


Fig. 14.— As in Fig. 13, but for models with  $\beta = 2$ ,  $D_c = 2$ , and a wind temperature of  $T_w = 57700$  K.



TABLE 1  
JOURNAL OF OBSERVATIONS

Observation Name	Spectrograph	Date	Observation Number	Duration (seconds)
WR 136	SWS06	1 Dec 1996	38101710	12872
WR 136	SWS01	1 Dec 1996	38101711	1140
WR 136 Off	SWS01	1 Dec 1996	38101712	1140

Table 2: Line Identifications

$\lambda$	Principal Line	Blends at $\Delta v$ ( $\text{km s}^{-1}$ )	Notes
2.83	He II 9-7	C IV 15-9 at +750	features near the blue and red wings are possibly weak He I and He II lines
3.09	He II 7-6	N III 8-7 at -390 C III 9-8 at -290 C IV 14-12 at 0  He II 11-8 at +350	the N line could be a significant contributor to the line flux  since He II 14-9 have emission at about 30% of $f_{cont}$ , this feature likely has a slight influence on the width of He II 7-6
3.15	He II 14-9	He II 19-10 at +560	blend may account for difficulty in matching the red wing width
3.74	He II 16-10	H I (Pf $\gamma$ ) at 0 He I 8-5 at 0	a sequence of transitions between different terms in the 8-5 line spread from -1000 to 0, which may account for the slight blue wing broadening
4.65	He II 14-10	H I (Pf $\beta$ ) at 0 He II 22-12 at +1225	
4.76	He II 8-7	He II 17-11 at -1350	
7.21	He II 14-11 <sup>(a)</sup>	He II 19-13 at +1460	

<sup>a</sup>We include 14-11 so that there are 3 lines with upper level 14. The 14-9 and 14-11 do not blend with H, but 14-10 does. In comparing the two with odd lower level, we can confirm whether the lines are thin. By comparing to the one with even lower level, we can infer the H/He ratio.

Table 3: He II Recombination Line Data for WR 136

Wavelength ( $\mu\text{m}$ )	Transition (He II)	HWHM <sup>a</sup> ( $\text{km s}^{-1}$ )	Continuum Flux (Jy)	EW ( $\text{\AA}$ )
2.826	9–7	1050	3.44	210
3.092	7–6	1090	3.20	790
3.145	14–9	1070	3.17	71
3.739	16–10	1050	2.79	97
4.652	14–10	1220	2.37	220
4.764	8–7	1170	2.32	570
7.208 <sup>b</sup>	14–11	—	—	180

<sup>a</sup> The HWHM is evaluated for the red wing.

<sup>b</sup> The He II 14–11 line and neighboring continuum are not sufficiently reliable to quote a line width or continuum flux value, although it is shown for the model line fits described in §3.3.4.

Table 4: Mass-Loss Rate Estimates for WR 136

Reference	$\dot{M}$ ( $10^{-5}M_{\odot}\text{yr}^{-1}$ )	Waveband	Flow Type
Abbott <i>et al.</i> (1986)	3.2	Radio free-free	smooth
Barlow & Cohen (1975)	2.3	Radio free-free	smooth
Crowther & Smith (1996)	12.5	NIR lines	smooth
Hamann & Koesterke (1998)	12.5	Optical/UV lines	smooth
Nugis <i>et al.</i> (1998)	6.25	Radio	clumped <sup>a</sup>

<sup>a</sup> These authors allow for clumping in their analysis, but conclude that the outer wind is unclumped.

Table 5: Adopted Parameters for WR 136

Parameter	Value
Subtype <sup>a</sup>	WN6
$d^b$	1.82 kpc
$T_*^c$	57700 K
$R_*^c$	$5R_{\odot}$
$L_*$	$2.5 \times 10^5 L_{\odot}$
$\dot{M}^d$	$6.25 \times 10^{-5} M_{\odot} \text{yr}^{-1}$
$v_{\infty}^e$	$1490 \text{ km s}^{-1}$
$T_w$	27,700–57,700 K
$X^f$	0.12

<sup>a</sup> From van der Hucht (2001).

<sup>b</sup> From Lundström & Stenholm (1984).

<sup>c</sup> From Crowther & Smith (1996) that are assumed for the base of the wind.

<sup>d</sup> From Nugis *et al.* (1998).

<sup>e</sup> From Paper I.

<sup>f</sup>  $X$  is the hydrogen mass-fraction.